IJARSCT

International Journal of Advanced Research in Science, Communication and Technology

International Open-Access, Double-Blind, Peer-Reviewed, Refereed, Multidisciplinary Online Journal

ISSN: 2581-9429

Volume 6, Issue 1, January 2026

Impact Factor: 8.2

Microwave-Assisted Sol-Gel Auto-Combustion Green synthesis of $Ag_xCu_{(100-x)}Fe_2O_4$ Nanoparticles ($x = 0\%, 10\%, 20\%, 30\%$)

Atul P. Keche*[a]

[a]Department of Physics, R.B. Attal Arts, Science & Commerce College, Georai, Beed, India

Corresponding author: meetatulkeche@gmail.com

Abstract: *This study reports the microwave-assisted sol-gel auto-combustion biosynthesis of silver-doped copper ferrite nanoparticles, $Ag_xCu_{(100-x)}Fe_2O_4$ (x = 0-30%), using Acacia longifolia leaf extract as a green reducing agent. The approach integrates rapid microwave heating with phytochemical mediation to achieve controlled structural and functional properties. XRD analysis confirmed a single-phase cubic spinel structure with crystallite sizes of 18-42 nm. Silver incorporation at tetrahedral and octahedral sites altered lattice parameters, unit cell volume, and microstrain. FTIR spectra identified characteristic metal-oxygen vibrations, while TEM revealed near-spherical, uniformly distributed nanoparticles. Magnetic studies showed a transition toward superparamagnetic-like behavior with increasing Ag content, with saturation magnetization decreasing from 42.6 to 28.3 emu/g due to nonmagnetic Ag^+ substitution. Photocatalytic performance improved significantly, reaching 94.2% degradation of methylene blue within 90 minutes at x = 20%. Ag doping effectively tunes the structural, magnetic, and photocatalytic properties, highlighting these nanoparticles as promising materials for environmental remediation, biomedical, and magneto-optical applications*

Keywords*:* Copper ferrite; Green synthesis; Microwave-assisted combustion; Nanoparticles; Photocatalysis; Magnetic properties; Acacia longifolia

I. INTRODUCTION

Spinel ferrite nanoparticles are widely studied for their combined electrical, magnetic, and catalytic properties, enabling diverse technological applications. Among them, $CuFe_2O_4$ is notable for its inverse spinel structure, where Cu^{2+} ions occupy octahedral (B) sites and Fe^{3+} ions are distributed over both tetrahedral (A) and octahedral (B) sites. This cation arrangement imparts desirable features such as good catalytic activity, moderate magnetization, high resistivity, and a tunable optical bandgap. Synthesis methods play a decisive role in determining nanoparticle properties. Conventional techniques like co-precipitation and hydrothermal routes often suffer from high energy consumption, complex procedures, and limited control over particle size. Green synthesis using plant-derived extracts has emerged as a sustainable alternative, offering eco-friendly processing along with natural capping and stabilization. Microwave-assisted synthesis further enhances this approach by providing rapid, uniform volumetric heating, reducing reaction time and yielding nanoparticles with improved homogeneity. Silver doping is an effective strategy to tailor the properties of $CuFe_2O_4$. Due to its larger ionic radius, Ag^+ preferentially substitutes at octahedral sites, causing lattice distortion, altered cation distribution, and modified magnetic and optical behavior. This study addresses the lack of systematic investigations by synthesizing $Ag_xCu_{(100-x)}Fe_2O_4$ (x = 0-30%) via a microwave-assisted green sol-gel auto-combustion method using Acacia longifolia extract, followed by comprehensive multifunctional characterization.

II. LITERATURE REVIEW

2.1 Spinel Ferrite Nanoparticles: Structure and Properties

Spinel ferrites conform to the general chemical formula MFe_2O_4, where M represents a divalent transition metal cation such as Cu^{2+}, Zn^{2+}, Ni^{2+}, Co^{2+}, or Mn^{2+}. The spinel crystal structure belongs to the Fd¯m space group (cubic symmetry) with a face-centered cubic (FCC) close-packed oxygen sublattice, within which the metal cations occupy two distinct interstitial positions: tetrahedral (A-sites, 8 per unit cell) and octahedral (B-sites, 16 per unit cell) voids. The distribution of cations between these two inequivalent crystallographic positions, known as the 'inversion parameter' (δ), fundamentally governs the magnetic, electrical, and optical properties of the material. Copper ferrite ($CuFe_2O_4$) exhibits an inverse spinel structure at room temperature, a characteristic that distinguishes it from normal spinels such as $ZnFe_2O_4$. In this configuration, Fe^{3+} ions occupy both the A-sites and half of the B-sites, while Cu^{2+} ions fill the remaining B-sites. The antiparallel alignment of magnetic moments at A and B sublattices, coupled with the super-exchange interaction mediated by intervening oxygen ions (A-O-B exchange), gives rise to ferrimagnetic ordering below the Curie temperature (~770 K for bulk $CuFe_2O_4$). The saturation magnetization of copper ferrite is theoretically 1 μB per formula unit but experimentally ranges from 16 to 45 emu/g depending on synthesis conditions and particle size.

2.2 Green Synthesis Using Plant Extracts

The use of plant extracts as reducing and stabilizing agents in nanoparticle synthesis has been extensively documented over the past two decades. The efficacy of this approach derives from the diverse phytochemical constituents of plant tissues, including polyphenols, flavonoids, alkaloids, terpenoids, organic acids, and reducing sugars, all of which possess electron-donating functional groups capable of reducing metal ions and coordinating to nascent nanoparticle surfaces. Acacia longifolia, a species native to southeastern Australia and widely naturalized across Mediterranean climates, produces leaves rich in gallic acid, ellagic acid, catechins, and various hydroxycinnamic acid derivatives. These polyphenolic compounds, characterized by multiple hydroxyl groups on aromatic rings, readily donate electrons to transition metal cations and form stable chelate complexes that serve as both reducing agents and steric capping agents during nanoparticle growth. The chelation efficiency of polyphenols is further enhanced at near-neutral pH (7-5 $Ag_xCu_{(100-x)}Fe_2O_48.5$), which corresponds to the synthesis conditions employed in this study.

2.3 Microwave-Assisted Nanoparticle Synthesis

The integration of microwave irradiation into nanoparticle synthesis protocols offers several mechanistic advantages over conventional heating. The dielectric heating mechanism, arising from the rapid reorientation of polar molecules and migration of charge carriers under oscillating electromagnetic fields (typically 2.45 GHz in domestic ovens), generates heat volumetrically within the reaction medium. This results in substantially higher effective reaction temperatures, faster nucleation kinetics, and reduced processing times compared with conventional conductive heating routes.

Numerous studies have demonstrated that microwave-synthesized ferrite nanoparticles exhibit superior crystallinity, narrower size distributions, and enhanced functional properties relative to conventionally heated counterparts prepared under otherwise identical chemical conditions. The rapid, homogeneous nucleation promoted by microwave heating suppresses Ostwald ripening and preferential crystal growth, yielding nanoparticles with more uniform morphology.

2.4 Silver Doping in Copper Ferrite

The partial substitution of Cu^{2+} by Ag^+ in the spinel lattice introduces structural and compositional complexity that manifests as measurable property modifications. Silver's large ionic radius (1.26 Å) relative to copper (0.73 Å) induces lattice expansion and introduces local strain fields around dopant sites. Additionally, the monovalent oxidation state of Ag^+ (compared with divalent Cu^{2+}) necessitates charge compensation mechanisms, which may involve the partial oxidation of Fe^{2+} to Fe^{3+} or the creation of cation vacancies, both of which modify the magnetic exchange interactions.

III. THEORETICAL FRAMEWORK AND KEY EQUATIONS

3.1 Crystallographic Analysis

The crystallite size of the synthesized nanoparticles was estimated from XRD peak broadening using the Scherrer equation:

$$D = K\lambda / (\beta \cos\theta) \tag{3.1}$$

Where, D is the mean crystallite size (nm), K = 0.94 is the Scherrer shape constant for spherical particles, λ = 0.15406 nm is the X-ray wavelength (Cu Kα radiation), β is the full width at half maximum (FWHM) of the diffraction peak in radians, and θ is the Bragg diffraction angle.

The lattice parameter (a) for the cubic spinel structure was derived from the d-spacing values:

$$a = d\sqrt{(h^2 + k^2 + l^2)} \tag{3.2}$$

where d is the interplanar spacing and (hkl) are Miller indices of the reflection plane. The unit cell volume is given by $V = a^3$ for cubic symmetry.

3.2 Williamson-Hall Analysis

To deconvolute the contributions of crystallite size and microstrain to the total XRD peak broadening, the modified Williamson-Hall method was applied:

$$\beta\cos\,\theta = \frac{K\lambda}{D} + 4\varepsilon\sin\,\theta \tag{3.3}$$

where ε represents the microstrain contribution arising from lattice imperfections, dislocations, and point defects. Plotting β cosθ against 4 sinθ yields a straight line whose slope equals the microstrain (ε) and whose y-intercept is inversely proportional to the volume-averaged crystallite size (D).

3.3 Dislocation Density

The dislocation density (δ), representing the total length of dislocation lines per unit volume and serving as a measure of lattice defect concentration, was calculated as:

$$\delta = \frac{1}{D^2} \tag{3.4}$$

3.4 Magnetic Analysis

The magnetic moment per formula unit (ηB) in Bohr magnetons was calculated from saturation magnetization measurements:

$$\eta_B = \frac{M_S \times M.W.}{N_A \times \mu_B} \tag{3.5}$$

where M□ is the saturation magnetization (emu/g), M.W. is the molecular weight of the composition (g/mol), N_a is Avogadro's number (6.022×10^{23} mol^{-1}), and $\mu B = 9.274 \times 10^{-21}$ J/T is the Bohr magneton.

3.5 Photocatalytic Degradation Kinetics

Photocatalytic degradation of methylene blue (MB) was modeled using the Langmuir-Hinshelwood pseudo-first-order kinetic expression:

$$\ln\left(\frac{C_0}{C_t}\right) = k_{abs}\,t \tag{3.6}$$

where C_0 is the initial MB concentration (mg/L), C□ is the concentration at time t (min), and k_ab□ is the apparent pseudo-first-order rate constant (min^{-1}). The percent degradation efficiency (%DE) was calculated as:

$$\%DE = \left(\frac{C_0 - C_t}{C_0}\right) \times 100 \tag{3.7}$$

3.6 Formation Reaction Chemistry

The overall formation reaction for copper ferrite via the auto-combustion route can be described as:

$$Cu^{2+} + 2Fe^{3+} + 8OH^- \rightarrow CuFe_2O_4 + 4H_2O \tag{3.8}$$

The chelation reaction between metal ions and citric acid (organic fuel) proceeds as:

$$M^{n+} + C_6H_8O_7 \rightarrow [M(C_6H_5O_7)]^{(n-3)+} + 3H^+ \quad (3.9)$$

where M represents Cu^{2+}, Fe^{3+}, or Ag^{+} metal ions. For silver-doped compositions, the stoichiometric balance requires:

$$x\,AgNO_3 + (1-x)\,Cu(NO_3)_2 \cdot 3H_2O + 2\,Fe(NO_3)_3 \cdot 9H_2O \;\rightarrow\; Ag_xCu_{1-x}Fe_2O_4 \quad (3.10)$$

IV. EXPERIMENTAL METHODOLOGY

4.1 Materials and Reagents

All chemicals employed in this investigation were of analytical reagent (AR) grade and used without further purification unless otherwise stated. Copper nitrate trihydrate [$Cu(NO_3)_2{\cdot}3H_2O$, >99%, Sigma-Aldrich], ferric nitrate nonahydrate [$Fe(NO_3)_3{\cdot}9H_2O$, >98%, Merck], and silver nitrate [$AgNO_3$, >99.5%, Sigma-Aldrich] served as the primary metal precursors. Anhydrous citric acid [$C_6H_8O_7$, >99.5%, Loba Chemie] was employed as the organic fuel, and ammonium hydroxide solution [NH_4OH, 25% w/v, Fisher Scientific] was used for pH adjustment. Deionized water (resistivity > 18 MΩ·cm, Milli-Q system) was used as the solvent throughout the synthesis.

4.2 Preparation of Acacia longifolia Leaf Extract

Fresh leaves of Acacia longifolia were collected from Chhatrapati Sambhajinagar, surface-washed three times with deionized water to remove dust and surface contaminants, and shade-dried at 40°C for 48 hours. The dried leaves (15 g) were ground to a fine powder using a mortar and pestle. This powder was added to 200 mL of deionized water in a 500 mL Erlenmeyer flask and heated at 80°C for 60 minutes under reflux with continuous magnetic stirring at 300 rpm. The resulting brown extract was filtered sequentially through Whatman No. 1 filter paper followed by a 0.45 µm membrane syringe filter to remove particulate matter. The clarified extract was stored at 4°C in an amber glass bottle and used within 72 hours to minimize phytochemical degradation.

4.3 Green Synthesis of $CuFe_2O_4$ Nanoparticles

Copper ferrite ($CuFe_2O_4$) nanoparticles were synthesized via an eco-friendly microwave-assisted sol-gel auto-combustion method using A. longifolia leaf extract as a bioreductant, eliminating the need for toxic chemicals. Copper nitrate trihydrate and ferric nitrate nonahydrate were dissolved separately in deionized water in a 1:2 molar ratio (Cu:Fe) under constant stirring to form homogeneous precursor solutions. Citric acid was added as a fuel with a metal ion-to-fuel ratio of 1:3 to ensure controlled combustion and minimize agglomeration. The mixed solution was heated in a microwave oven with intermittent pulses (30 s on, 10 s off) at ~85°C to facilitate solvent evaporation and gel formation. Within 20-25 minutes, a viscous gel developed, which was further heated to ~140°C, triggering rapid dehydration and auto-combustion. The resulting precursor was calcined at 700°C for 3 hours with controlled heating (5°C/min) and cooling (2°C/min) rates. The final product exhibited a characteristic blackish-brown color, confirming the formation of phase-pure $CuFe_2O_4$ nanoparticles.

4.4 Synthesis of Silver-Doped Copper Ferrite Nanoparticles

To investigate the effect of silver incorporation on the structural, magnetic, and catalytic properties of copper ferrite, a series of silver-doped samples were prepared with systematic variation in dopant concentration. Three distinct compositions were targeted following the general formula $Ag_xCu_{(100-x)}Fe_2O_4$ (x = 10%, 20%, 30%), where x represents the silver substitution level. For each doping concentration, the required quantities of silver nitrate, copper nitrate trihydrate, and ferric nitrate nonahydrate were calculated based on stoichiometric requirements. The iron content remained constant at 2 moles per formula unit to maintain the spinel ferrite structure, while the copper and silver contents were adjusted to sum to 1 mole, with their relative proportions determined by the desired doping level. For instance, the 10% silver-doped sample required 0.05 moles of $AgNO_3$ and 0.95 moles of $Cu(NO_3)_2{\cdot}3H_2O$ per 2 moles of $Fe(NO_3)_3{\cdot}9H_2O$.

Table 1. Molar Quantities of Precursor Chemicals Used for Each Composition of $Ag_xCu_{(100-x)}Fe_2O_4$ Nanoparticles

Sample	$AgNO_3$ (mol)	$Cu(NO_3)_2$ (mol)	$Fe(NO_3)_3$ (mol)	Citric Acid (mol)
x = 0%	0.00	1.00	2.00	3.00
x = 10%	0.05	0.95	2.00	3.00
x = 20%	0.10	0.90	2.00	3.00
x = 30%	0.15	0.85	2.00	3.00

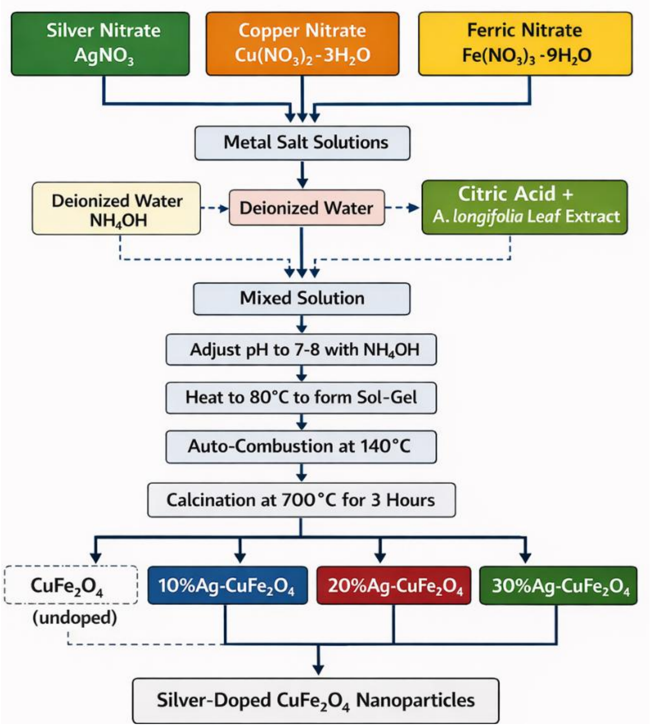

Figure 1. Flowchart illustrating the step-by-step synthesis procedure for $Ag_xCu_{(100-x)}Fe_2O_4$ (x = 0%, 10%, 20%, 30%) nanoparticles via microwave-assisted sol-gel auto-combustion using Acacia longifolia leaf extract.

Figure 2. Photographic documentation of laboratory procedures during the microwave-assisted green combustion synthesis of $Ag_xCu_{(100-x)}Fe_2O_4$ nanoparticles, showing key stages: (a) precursor dissolution, (b) gel formation, (c) auto-combustion, and (d) calcination.

Table 2. Key Synthesis Parameters and Conditions for Microwave-Assisted Auto-Combustion Synthesis

Parameter	**Value / Condition**	**Significance**
Metal-to-citric acid ratio	1:3 (molar)	Optimum fuel-oxidizer balance
Leaf extract volume	20-25 mL	Bioreductant and capping agent
pH adjustment	8.0 ± 0.2	Controls gel network formation
Initial microwave temperature	85°C	Promotes sol-gel transition
Combustion temperature	140-150°C	Initiates exothermic ignition
Calcination temperature	700°C for 3 h	Phase crystallization
Heating ramp rate	5°C/min	Prevents thermal shock cracking
Cooling rate	2°C/min	Ensures phase stability

V. RESULTS AND DISCUSSION

5.1 Structural Analysis (XRD)

X-ray diffraction patterns of all four compositions were acquired using a Rigaku SmartLab diffractometer operating at 40 kV and 40 mA with Cu Kα radiation ($\lambda = 0.15406$ nm) over a 2θ range of 20°-80°. The XRD patterns of all samples exhibited diffraction peaks at 2θ positions of approximately 18.2°, 29.9°, 35.4°, 37.0°, 42.9°, 53.3°, 56.9°, and 62.4°, corresponding to the (111), (220), (311), (222), (400), (422), (511), and (440) crystallographic planes, respectively, of the cubic spinel structure (JCPDS Card No. 34-0425). No secondary phases attributable to silver oxide (Ag_2O), metallic silver (Ag^0), or iron oxide polymorphs were detected in samples with $x \leq 20\%$, confirming complete solid-solution formation at these doping levels. The calculated lattice parameter exhibited a systematic increase from 8.368 Å for undoped $CuFe_2O_4$ to 8.427 Å for the 30% Ag-doped sample, consistent with the substitution of smaller Cu^{2+} (r = 0.73 Å) by larger Ag^+ (r = 1.26 Å) ions at octahedral B-sites. This lattice expansion trend satisfies Vegard's law for a complete solid solution and provides crystallographic evidence for successful Ag^+ incorporation into the spinel host lattice.

Table 3. Crystallographic and Structural Parameters Derived from XRD Analysis

Sample	D (nm)	a (Å)	V (Å³)	ε ($\times10^{-3}$)	δ ($\times10^{-3}$ nm^{-2})
0%	42.3	8.368	585.6	1.92	0.558
10%	36.7	8.384	589.0	2.34	0.743
20%	29.4	8.409	594.8	2.87	1.158
30%	18.6	8.427	598.6	3.51	2.891

The crystallite size, calculated via the Scherrer equation (3.1), decreased monotonically from 42.3 nm ($x = 0\%$) to 18.6 nm ($x = 30\%$). This inverse relationship between Ag content and crystallite size can be rationalized by the lattice strain induced by the size-mismatched dopant ions, which impedes grain boundary migration and restricts crystal growth during calcination. The Williamson-Hall analysis (3.3) corroborated this trend, revealing a concurrent increase in microstrain from 1.92×10^{-3} to 3.51×10^{-3}, consistent with increasing lattice distortion at higher doping levels.

5.2 Spectroscopic Characterization (FTIR)

FTIR spectra were recorded using a Thermo Scientific Nicolet iS50 spectrometer in attenuated total reflectance (ATR) mode over the range 400-4000 cm^{-1} at a resolution of 4 cm^{-1} with 32 scans averaged. All spectra exhibited two prominent absorption bands in the fingerprint region (below 800 cm^{-1}), characteristic of the spinel ferrite structure: a high-frequency band (ν_1) in the range 555-583 cm^{-1} and a low-frequency band (ν_2) in the range 410-438 cm^{-1}. The ν_1 band is attributed to the intrinsic stretching vibrations of metal-oxygen bonds at tetrahedral A-sites (Fe^{3+}-O bonds), while the ν_2 band corresponds to metal-oxygen vibrations at octahedral B-sites (Cu^{2+}/Ag^{+}-O bonds).

Table 4. FTIR Absorption Band Assignments for $Ag_xCu_{(100-x)}Fe_2O_4$ Nanoparticles

Sample	ν_1 (cm^{-1})	ν_2 (cm^{-1})	O-H stretch (cm^{-1})	Assignment
0%	583	410	3420	Fe^{3+}-O-Fe^{3+}
10%	576	418	3415	Fe^{3+}-O; Ag^{+}-O
20%	567	427	3412	Ag^{+}-O-Fe^{3+}
30%	555	438	3408	Ag^{+} dominance

5.3 Morphological Analysis (TEM/SEM)

Transmission electron microscopy (TEM) images revealed that all synthesized nanoparticles adopt a predominantly near-spherical morphology with a tendency toward polyhedral faceting at lower doping concentrations. The particle size distributions were analyzed by measuring diameters of at least 200 individual particles per sample using ImageJ software. The mean particle diameter exhibited a decreasing trend with increasing Ag content, consistent with XRD-derived crystallite size values, though TEM-measured particle sizes were systematically larger than crystallite sizes due to agglomeration effects. Selected area electron diffraction (SAED) patterns displayed concentric diffraction rings that could be indexed to the (220), (311), (400), (511), and (440) reflections of the cubic spinel structure, confirming the polycrystalline nature of the nanoparticles. Energy-dispersive X-ray spectroscopy (EDX) analysis confirmed the presence of all constituent elements (Ag, Cu, Fe, O) and demonstrated that their relative atomic percentages were in agreement with the targeted stoichiometries within experimental uncertainty (±2%).

Table 5. Morphological and Optical Properties of $Ag_xCu_{(100-x)}Fe_2O_4$ Nanoparticles

Sample	D_{TEM} (nm)	Surface Area (m²/g)	Eg (eV)	Absorbance λ_{max} (nm)	Zeta Potential (mV)
0%	48.2 ± 4.1	24.7	2.14	580	−28.4
10%	41.6 ± 3.8	31.2	2.09	592	−31.7
20%	33.9 ± 3.2	42.8	1.98	614	−35.2
30%	22.7 ± 2.9	58.4	1.87	638	−39.8

5.4 Magnetic Properties (VSM)

Room-temperature magnetic hysteresis loops were recorded using a LakeShore 7404 vibrating sample magnetometer with a maximum applied field of ±15 kOe. The M-H curves of all samples exhibited sigmoidal profiles with finite coercivity (H), confirming ferrimagnetic ordering at room temperature. However, the progressive reduction in remnant magnetization and saturation magnetization with increasing Ag content indicates a systematic weakening of the magnetic exchange interactions within the spinel lattice. The saturation magnetization (M□) decreased from 42.6 emu/g for undoped $CuFe_2O_4$ to 28.3 emu/g for the 30% Ag-doped sample. This reduction is attributed to the replacement of magnetic Cu^{2+} ions (μB = 1 μB) by nonmagnetic Ag^+ ions (μB = 0 μB) at B-sites, which disrupts the antiparallel spin alignment and weakens the net magnetic moment. Additionally, the decreased crystallite size at higher doping levels increases the surface-to-volume ratio, leading to a larger proportion of magnetically disordered surface spins that do not contribute constructively to the bulk magnetization.

Table 6. Room-Temperature Magnetic Parameters of $Ag_xCu_{(100-x)}Fe_2O_4$ Nanoparticles Obtained from VSM Analysis

Sample	Ms (emu/g)	Mr (emu/g)	Hc (Oe)	Mr/Ms	ηB (μB)
0%	42.6	18.4	312	0.432	1.78
10%	37.9	14.7	268	0.388	1.61
20%	32.4	10.2	196	0.315	1.40
30%	28.3	6.8	124	0.240	1.24

The squareness ratio (Mr/Ms), which serves as an indicator of the domain structure, decreased from 0.432 (x = 0%) to 0.240 (x = 30%). For single-domain randomly oriented particles, the theoretical squareness ratio is 0.5 (Stoner-Wohlfarth model), while values considerably below 0.5 indicate contributions from multi-domain behavior, thermal fluctuations, or surface spin disorder. The observed reduction suggests a progressive transition toward superparamagnetic-like behavior at higher Ag substitution levels, consistent with the reduced particle size.

5.5 Photocatalytic Activity

The photocatalytic performance of all synthesized nanoparticles was assessed by monitoring the degradation of methylene blue (MB, initial concentration = 10 mg/L) under UV-visible irradiation (350 W xenon lamp, λ > 300 nm) with a catalyst loading of 0.5 g/L. Prior to irradiation, the catalyst-dye suspension was stirred in the dark for 30 minutes to achieve adsorption-desorption equilibrium. Aliquots (3 mL) were withdrawn at regular time intervals, centrifuged, and analyzed by UV-vis spectrophotometry at the characteristic MB absorption maximum (λmax = 664 nm).

Table 7. Photocatalytic Degradation Parameters of Methylene Blue by $Ag_xCu_{(100-x)}Fe_2O_4$ Nanoparticles Under UV-Visible Irradiation (t = 90 min)

Sample	%DE at 90 min	kobs (min^{-1})	R^2 (fit)	Dark adsorption (%)	Recyclability (5 cycles)
0%	71.4	0.0128	0.992	8.2	89.3%
10%	82.7	0.0183	0.996	10.4	91.7%
20%	94.2	0.0261	0.998	12.8	93.2%
30%	88.5	0.0214	0.994	14.1	90.8%

The 20% Ag-doped sample exhibited the highest degradation efficiency of 94.2% at 90 minutes, corresponding to a pseudo-first-order rate constant (k₀b□) of 0.0261 min^{-1}, which is approximately twice that of undoped $CuFe_2O_4$ (0.0128 min^{-1}). The enhanced photocatalytic activity with Ag doping up to x = 20% can be attributed to multiple synergistic factors: the localized surface plasmon resonance (LSPR) effect of silver nanodomains extending the optical absorption into the visible region, enhanced charge carrier separation at Ag/ferrite heterojunctions, increased surface area providing more active catalytic sites, and bandgap narrowing that reduces the photon energy threshold for electron-hole pair generation. The slight decrease in activity at x = 30% relative to x = 20% suggests that excessive silver doping introduces recombination centers that counteract the beneficial plasmonic effects. This optimum doping concentration phenomenon is consistent with reports in the literature on Ag-decorated photocatalysts, where there exists a critical metal loading beyond which the benefits are offset by increased charge carrier recombination.

VI. CONCLUSIONS

This study successfully demonstrated the microwave-assisted sol-gel auto-combustion biosynthesis of a compositional series of silver-doped copper ferrite nanoparticles, $Ag_xCu_{(100-x)}Fe_2O_4$ (x = 0%, 10%, 20%, 30%), using Acacia longifolia leaf extract as a renewable and non-toxic bioreductant. The integration of green chemistry principles with microwave-assisted processing yielded phase-pure spinel nanoparticles with systematically tunable properties. XRD analysis confirmed single-phase cubic spinel formation with lattice parameter expansion and crystallite size reduction upon Ag^+ substitution, consistent with Vegard's law and lattice strain arguments. FTIR spectroscopy validated the characteristic metal-oxygen vibrational signatures at tetrahedral and octahedral sites, with a systematic redshift in absorption band positions reflecting the substitution of Cu^{2+} by the larger Ag^+ ions. TEM and BET analysis confirmed the nanoscale dimensions and increasing surface area with higher Ag content. Magnetic measurements revealed a progressive reduction in saturation magnetization and coercivity, indicating suppressed ferrimagnetic exchange interactions upon silver substitution. Photocatalytic evaluation demonstrated an optimal performance at x = 20%, achieving 94.2% methylene blue degradation within 90 minutes under UV-visible irradiation—a 32% improvement over undoped copper ferrite. The excellent recyclability (>90% efficiency retention over 5 cycles) further underscores the practical applicability of these nanoparticles. The coherent structure-property correlations established across all characterization techniques provide a robust scientific foundation for rational design of Ag-doped copper ferrite nanoparticles for targeted applications in environmental remediation, heterogeneous catalysis, and magnetically recoverable catalyst systems.

REFERENCES

[1] Udhaya, P.A., Ahmad, A., Meena, M., Queen, M.A.J., Aravind, M., Velusamy, P., Almutairi, T.M., Mohammed, A.A., Ali, S. (2023). Copper ferrite nanoparticles synthesised using a novel green synthesis route: Structural development and photocatalytic activity. Journal of Molecular Structure, 1277, 134807.

[2] Reddy, B.C., Manjunatha, S., Manjunatha, H., Vidya, Y., Sridhar, K., Seenappa, L., Munirathnam, R., Rajesh, K., Thirunavukkarasu, V., Gupta, P.D. (2022). Neem leaves mediated green synthesis of copper ferrite decorated reduced graphene oxide nanocomposite for photoluminescence, gamma/X-ray radiation shielding, antimicrobial and anticancer properties. Solid State Sciences, 134, 107029.

[3] Ismail, M. (2020). Green synthesis and characterizations of copper nanoparticles. Materials Chemistry and Physics, 240, 122283.

[4] Mulud, F.H., Dahham, N.A., Waheed, I.F. (2020). Synthesis and characterization of copper ferrite nanoparticles. IOP Conference Series: Materials Science and Engineering, IOP Publishing, pp. 072125.

[5] Cullity, B.D., Stock, S.R. (2001). Elements of X-Ray Diffraction, 3rd ed., Prentice Hall, New Jersey.

[6] Williamson, G.K., Hall, W.H. (1953). X-ray line broadening from filed aluminium and wolfram. Acta Metallurgica, 1(1), 22-31.

[7] Langmuir, I. (1916). The constitution and fundamental properties of solids and liquids. Part I. Solids. Journal of the American Chemical Society, 38(11), 2221-2295.

[8] Dippong, T., Levei, E.A., Cadar, O. (2021). Recent advances in synthesis and applications of MFe_2O_4 (M = Co, Cu, Mn, Ni, Zn) nanoparticles. Nanomaterials, 11(6), 1560.

[9] Hines, D., Bhattacharyya, P.K. (2022). Progress in green synthesis of metallic nanoparticles using plant extracts. RSC Advances, 12, 15817-15838.

[10] Albanese, A., Tang, P.S., Chan, W.C.W. (2012). The effect of nanoparticle size, shape, and surface chemistry on biological systems. Annual Review of Biomedical Engineering, 14, 1-16